February 2, 1999

Multiple Components in the Millimeter Emission of a Solar Flare

J.-P. Raulin[1], S. M. White and M. R. Kundu
Astronomy Department, University of Maryland, College Park, MD 20742

A. V. R. Silva[1]
California Institute of Technology, Pasadena, CA 91125

and

K. Shibasaki
Nobeyama Radio Observatory, Nobeyama, Minamimaki, Minamisaku, Nagano 384-13, Japan

ABSTRACT

We analyze a small flare using imaging data at millimeter, microwave and soft X–ray wavelengths, and microwave and hard X–ray spectral observations. The remarkable aspect of this flare is evidence for the presence of MeV–energy electrons, which are responsible for the nonthermal millimeter emission, at a time when no hard X–rays from lower–energy electrons are detected. This occurs during a smoothly varying phase which is seen at radio wavelengths to last several minutes and is the brightest phase at millimeter wavelengths, but is undetected in hard X–rays: it follows a brief spike of emission at flare onset which has the more usual properties of impulsive events and features nonthermal microwave, millimeter and hard X–ray emission. We interpret the phase which is brightest at millimeter wavelengths as due to efficient trapping of a relatively small number of nonthermal electrons, whereas during the hard X–ray emission trapping is much less efficient and the decay time is much shorter at all energies, leading to a larger ratio of hard X–ray flux to radio flux. As in many previous events studied at millimeter wavelengths, there is a discrepancy

[1]present address: CRAAE, Instituto Presbiteriano Mackenzie, Rua de Consolação, 896, 01302–000 São Paulo, SP, Brazil

between the electron energy spectral indices inferred from the milllimeter and hard X–ray data during the impulsive phase when both are detected: again it appears that the energy spectrum at 1 MeV must be significantly flatter than at several hundred keV and below. However, there are problems in reconciling quantitatively the energy spectra for the hard–X–ray–emitting and radio–emitting components: based on the most plausible parameters the radio–emitting electrons should produce most of the hard X–rays. One solution to this contradiction is to invoke a coronal magnetic field stronger than seems likely based on the photospheric magnetic field.

Subject headings: Sun: activity, corona, flares, radio radiation, X-ray

1. INTRODUCTION

The development of millimeter arrays such as the Berkeley Illinois Maryland Array (BIMA) in recent years has made it possible to carry out high spatial resolution observations of solar flares at millimeter wavelengths. Millimeter emission in flares is produced both by the highest energy electrons accelerated by solar flares, and by chromospheric material heated to X–ray emitting temperatures by the deposition of energy from nonthermal electrons (e.g., White & Kundu 1992). The first high sensitivity interferometric observations at 86 GHz using BIMA were reported by Kundu et al. (1990). These were made with a 3–element interferometer which did not permit snapshot imaging. This paper continues the analysis of flares observed by BIMA in August 1994 which are the first set of events for which true high–spatial–resolution images can be made; two of these events have previously been analyzed by Silva et al. (1996, 1997).

In the impulsive phase the millimeter emission of flares is due to gyrosynchrotron emission of MeV–energy electrons in coronal magnetic fields, and thus millimeter observations provide a diagnostic of electrons with energies higher than those which generally produce hard X–rays ($\sim$ 50 – 200 keV) or microwave emission ($\gtrsim$ 200 keV). Millimeter emission can be used in conjunction with other radio data to determine the energy spectral index of the radiating electrons, and this may be compared with indices derived from other diagnostics such as hard X–ray spectra. A confident determination of both hard X-ray and radio spectral indices is necessary in order to determine whether hard X-ray and radio emissions come from the same population of accelerated electrons. In a number of observations it has been inferred that the energy distribution of millimeter–emitting electrons is harder than that of the electrons producing hard X-rays and microwaves in the same flares (Kundu et al. 1994, Silva et al. 1997). Occasionally flares have been observed to show breaks in their hard X–ray spectra such that the higher–energy electrons have a harder spectrum (Dennis 1985, Vilmer 1997). Often there is inadequate spectral coverage in hard X-rays or microwaves to make a firm comparison (e.g., Alissandrakis 1986, Staehli, Gary & Hurford 1989), but additional clues may be found from a close examination of the time profiles observed at different wavelengths during the impulsive phase of solar flares (Lim et al. 1992, Kundu et al. 1994).

In this paper we report imaging millimeter observations of a small solar flare observed in the hard X-ray, microwave and millimeter domains. The remarkable feature of this event is the presence of several components in the radio emission with quite distinct properties. We identify these components with distinct energetic populations present during different stages of the event. The next section describes the observational results. Section 3 is devoted to the interpretation of the radio and X–ray emissions. We compare the temporal evolution of the impulsive phase of the flare at different wavelengths, and discuss the implications for the electron energy distribution. There has been a long history of attempts to reconcile the hard X–ray–emitting and radio–emitting electron energy distributions ever since the realization that the two emissions both come from energetic electrons (Kundu 1961). In this event the simplest assumptions based on the available data do not lead to a self–consistent picture for the two electron populations, and we explore ways in which the radio and hard X–ray data can be reconciled. In section 4 we present our conclusions.

2. OBSERVATIONS

The event reported in this paper occurred in AR 7765 on August 16, 1994, at 23 UT (all times given in this paper will be in UT). The active region was located in the southeast quadrant of the Sun's disk. No Hα flare emission was reported in AR 7765 between August 16 18:00 UT and August 17 01:00 UT. The event we are interested in was detected by the soft X–ray detectors on the Geostationary Operational Environmental Satellites (GOES), and was classified as a B5.6 X-ray flare with peak emission at 23:12 UT. The flare was simultaneously detected by the Berkeley Illinois Maryland Array (BIMA) at 86 GHz (3.5 mm), the Nobeyama Radioheliograph (NRO) at 17 GHz (17.5 mm), the Nobeyama microwave polarimeters (1.0, 2.0, 3.75, 9.4 and 17 GHz), and the Owens Valley Radio Observatory frequency–agile interferometer at 45 frequencies between 1 and 18 GHz. The soft X-ray and hard X-ray telescopes (SXT and HXT) on the *Yohkoh* satellite were in satellite night during the impulsive phase of the flare and SXT imaging data are not available until 23:14 UT, during the gradual decay phase of the flare. Finally the Large

Area Detectors of the BATSE instrument on the Compton Gamma Ray Observatory (CGRO-BATSE) also detected the flare above 25 keV.

In order to clarify the subsequent discussion, in Figure 1 we present the time profiles of the impulsive phase of this event in hard X–rays and at microwave and millimeter wavelengths. This figure demonstrates that there were two distinct periods within the impulsive phase: a "normal" impulsive spike from 23:03:36 to 23:04:20 UT during which the hard X–rays, microwaves and millimeter emission all have similar profiles, which we will henceforth call the "hard X–ray phase"; and a period from 23:04:20 to 23:07:00 UT during which radio emission is detected and millimeter emission in particular is strong, but with no detectable accompanying hard X–rays: we will henceforth call this the "millimeter" phase. As we will discuss later, a gradual decay phase dominated by thermal emission follows the impulsive phase and lasts until $\sim$ 23:40 UT.

2.1. Radio Observations

2.1.1. BIMA Observations

At the time of the flare BIMA was operating with only four of the six antennae in the array available, allowing a total of six baselines varying in length from 12 to 52 m (projected lengths at the time of the flare were 12 to 42 m). These baselines provide spatial Fourier components of the sky brightness distribution with the corresponding fringe spacings in the range $17''$ - $60''$ at the wavelength of 3.5 mm; the size of the synthesised beam in the images constructed from the data was $18'' \times 7''$ at the time of the the flare. For details of the BIMA instrument the reader is refered to Welch et al. (1996).

With just six baselines, only limited mapping of snapshot data can be carried out. In particular, there is some ambiguity in the source position on the scale of the longest fringe spacing. Deconvolution was carried out in the standard MIRIAD package. The dirty BIMA map shows a "wallpaper" pattern of possible source locations separated by $\sim$ $60''$ in the east–west direction and $\sim$ $100''$ in the north–south direction. We selected the location closest to the active region position and "cleaned" the images using conventional techniques by searching for flux in a box of size $\sim$ $60''$ around this location. If there was no significant emission outside this $60''$ box, the maps should adequately represent the emission present. The cleaned images did not show any evidence for poorly deconvolved structures which might result from more distant flux. At the time of the observations an error in the telescope pointing software resulted in the telescope being pointed $20''$ west of the intended location, and the data have been shifted in phase accordingly to correct for this effect. Apart from the straightforward position shift, the effect on the data of this offset is negligible (the primary beam FWHM is $\sim 140''$).

We carried out a pre–flare subtraction of the data in order to improve the quality of the flare maps. Ideally this would be carried out by mapping the non–flare data over the whole observation to produce a model of the active region emission which could be subtracted from the flare data (at these short wavelengths the millimeter emission of all except the largest flares is optically thin and so is simply an addition to the non–flare emission from the optically–thick chromosphere and the optically–thin corona). However, with 6 baselines we are unable to produce a satisfactory model for the non–flare emission. We have therefore subtracted an average over several minutes of the pre–flare visibilities on each baseline before making flare maps. Only on the shortest baselines is the pre–flare flux a significant fraction of the flare emission, and on these short baselines the non–flare emission changes only slowly due to earth rotation. In this paper we emphasize the first few minutes of the flare, and inspection of the subtracted data indicates that there are no significant phase drifts due to the atmosphere or earth rotation during this period. Amplitudes have been corrected for the 13 dB of attenuation applied in the second IF to keep the system from saturating. Because of the non–standard nature of solar observing at BIMA, we estimate the uncertainty in the absolute calibration of BIMA solar data to be $\sim 50\%$ (the relative calibration of the different antennas is much better than this). This relatively large uncertainty in the 86 GHz flux leads to an uncertainty from -0.4 to +0.2 in the calculated radio spectral index from 15 to 86 GHz.

Figures 2a and 2b show the preflare–subtracted flux density detected on the longest and shortest BIMA baselines, respectively (baselines 4-7 and 6-7, with lengths 52 and 12 m). In these plots we can clearly distinguish the impulsive phase of roughly 4 minutes (23:03:36 - 23:08:00 UT, including both the "hard X–ray" and "millimeter" phases mentioned earlier), and the gradual phase starting at about 23:08 UT and extending up to 23:40 UT with a maximum at around 23:20 UT. The gap between 23:25:48 and 23:32:06 UT corresponds to a calibration observation. It is apparent from Figs. 2a-b that the ratio of the flux measured on the shortest baseline to that measured on the longest baseline changes dramatically during the event: in the gradual phase the ratio is large, indicating a source size large compared to the fringe spacing on the longest baseline, whereas in the impulsive phase the ratio is much smaller, indicating a smaller source. For comparison, Fig. 2c plots the GOES soft X–ray flux for the same period. The soft X–ray emission begins to increase rapidly at the start of the impulsive phase and peaks at around 23:12 UT, well after the millimeter peak in the impulsive phase but well before the millimeter peak in the gradual phase.

On the longest baseline (Fig. 2a) a very brief impulsive spike may be seen at 23:03:55

UT which is barely evident on the shortest baseline (Fig. 2b). The ratio of the flux densities observed at 23:03:55 UT (peak of the hard X–ray phase) and at 23:04:48 UT (peak of the millimeter phase seen by BIMA) increases with the length of the baseline, suggesting that the millimeter source size is smaller during the hard X–ray phase than during the millimeter phase. The hard X–ray phase is not well defined in the temporal evolution of the shortest baseline at BIMA because the large pre–flare flux on the short baseline combined with atmospheric phase fluctuations during the late summer afternoon and pointing problems due to wind, which particularly affect antenna 3, effectively result in a large noise level on short baselines which masks some of the weak impulsive emission.

In order to determine the physical parameters of the millimeter emission, we assume that the flare source has a Gaussian spatial brightness distribution and perform a fit to the visibilities to determine the total flux and the source size. To reduce the number of free parameters, the source is assumed to be the same size in both dimensions. This assumption may not be correct and accordingly the sizes derived represent a mean dimension of the source in some sense, but with just six baselines we have insufficient information to fit more parameters reliably. The total flux density of the millimeter source determined from the fits is plotted in Fig. 2d (points with error bars) and is in good agreement with the temporal evolution of the flux on the shortest baseline (Fig. 2b), as expected.

The time evolution of the size (FWHM) of the radio source is shown in Fig. 2e. It is $\sim 7''$ during the impulsive phase but increases to $\sim 12''$ during the gradual decay phase. Finally, in Fig. 2f we have plotted the temporal evolution of the source brightness temperature T_b, which has been computed from the source flux and size using the standard definition

$$T_b = (\frac{c^2}{2k\nu^2}).(\frac{S_\nu}{\Omega}) \tag{1}$$

where Ω is the solid angle subtended by the radio source. T_b ranges from 13000 K at the peak of the millimeter phase to several thousand K during the gradual decay phase.

2.1.2. Nobeyama and OVRO Observations

Figure 3 compares the radio flux densities observed by the BIMA interferometer at 86 GHz, the NRO radioheliograph at 17 GHz (the radioheliograph "correlation coefficient", which represents the flux in compact structures, converted to sfu by comparison with simultaneous calibration images at discrete times), and the OVRO 3.4, 7.0 and 9.0 GHz data (the correlated flux measured by the two 27m dishes, preflare–subtracted). The microwave time profiles are markedly different from the millimeter time profile in that the brightest emission occurs during the hard X–ray phase at 23:04 UT. The millimeter phase (peaking at 23:05 UT) is relatively less bright in microwaves, appearing more as a "shoulder" in the decay of the hard X–ray phase emission than as a separate component.

Images of the flare radio emission at 17 GHz from the Nobeyama radioheliograph show a source which is compact on the scale of the beam size (which is $\sim 12''$: see Fig. 5, discussed further below). The brightness temperature reached 1.8 $\times 10^6$ K. The images show weak circular polarization ($\sim$ 5%) at 17 GHz during the hard X–ray phase of the flare, which diminishes to less than 1% during the gradual decay phase after 23:10 UT. The polarization maps suggest that the 17 GHz source is bipolar, being of positive polarity (corresponding to upgoing magnetic fields) to the north–west and negative polarity to the south–east. During the rise of the hard X–ray phase the negative polarity component is stronger, but from 23:03:50 UT onwards the positive polarity dominates.

2.1.3. Radio Spectrum

In Figure 4 we plot the radio spectrum at three different times: at the peak of the hard X–ray phase, 23:03:59 UT; at the peak of the millimeter phase, 23:04:59 UT; and at the peak of the millimeter emission in the gradual decay phase, 23:17:59 UT. Due to minor discrepancies at the time of the microwave peak (23:04 UT) between the OVRO high–frequency data and both the Nobeyama 9.4 and 17 GHz polarimeter data and the 17 GHz radioheliograph fluxes (which agree with one another), we do not plot the OVRO data above 7 GHz. The cause of this discrepancy is not understood, but it does not affect our analysis in any way. The OVRO and Nobeyama polarimeter data agree with one another at the lower frequencies in common to both sites at the time of the microwave peak, and at 9.4 GHz at later times during the event (e.g., 23:05 UT).

The differences in the spectra are clearly evident: during the hard X–ray phase the spectrum is much steeper on the optically–thin high–frequency side than it is 1 minute later during the peak of the millimeter phase; and in the gradual decay phase the spectrum is essentially flat, as expected for optically–thin free–free emission from the soft–X–ray–emitting post–flare loops.

Using the averaged flux density of the radio emission at 17 and 86 GHz we have determined the high frequency slope (α) of the radio spectrum at different times during the event. Both the OVRO and Nobeyama polarimeter data clearly indicate that the spectral peak (ν_{peak}) is well below 17 GHz. This ensures that 17 GHz and higher frequencies belong to the optically thin part of the spectrum. We note also that ν_{peak} does not vary greatly during the impulsive phase. During the impulsive phase of the flare $-\alpha$ decreases from 1.75 to 1, with a value of 1.66 at the peak of the hard X–ray phase. If we use the standard gyrosynchrotron approximation for the relation between the energy spectral index and the radio flux spectral index, $\alpha = 1.22 - 0.9\delta_r$ (Dulk & Marsh 1982), to compute an approximate electron energy spectral index δ_r from the radio flux spectral index α, we find that the electron spectral index varies from 3.3 to 2.5 during the impulsive phase, with a value of 3.2 at peak of the hard X–ray phase.

2.2. X-ray Observations

2.2.1. Soft X-ray Observations

The GOES data for the 1-8 Å (lower–energy) channel are plotted in Figure 2c. We have converted the GOES soft X–ray data in the two channels (1-8 Å and 0.5-4 Å) into physical properties (temperature T_e and emission measure EM) of the soft X-ray emitting plasma using the expressions of Thomas et al. (1985). T_e reaches a maximum of 8.7 $\times 10^6$ K near the end of the impulsive phase at 23:07 UT. At this time the value of EM is 5 $\times 10^{47}$ cm^{-3}. Later, at around 23:20 UT, EM reaches its maximum of 1.6 $\times 10^{48}$ cm^{-3} when the temperature is T_e = 5.5 $\times 10^6$ K. This is later than the peak in the 1-8 Å count rate and closer to the time of the maximum of the gradual phase observed at 86 GHz.

As mentioned above, the impulsive phase of the flare occurred during spacecraft night for the *Yohkoh* satellite. Observations resumed at 23:15 UT during the gradual decay phase. Figure 5 shows a preflare SXT image of the active region (a, 21:26 UT) and an image obtained close to the peak of the gradual phase which is dominated by a bright post–flare loop (b, 23:16 UT). The dashed and full lines on panels a and b are contours of the photospheric magnetic field observed at KPNO on the following day (Aug. 17) at 17:19 UT (no magnetogram is available for the 16th; we have rotated the magnetogram for the 17th back to the appropriate time). We note that additional flares occurred between the time of this event and the time of the magnetogram, suggesting ongoing evolution of the magnetic field in the active region, and it is possible that the magnetogram shown does not accurately represent the magnetic field configuration at the time of our event. In Figs. 5c and 5d we plot contours of the BIMA radio source during the impulsive and gradual phases, respectively, overlaid on the SXT post–flare image. The 86 GHz source appears to be associated with either the northern footpoint or the looptop, but there is enough uncertainty in the 86 GHz source position that we cannot further decide between these two interpretations. Figures 5e and 5f show the contours of the Nobeyama 17 GHz flare images at the corresponding times, again overlaid on the SXT post–flare image. We note that the SXT post–flare loop is located slightly north of the brightest soft X-ray structure in the pre–flare image, which however was obtained some 90 minutes prior to the flare. The relatively small size of the soft X–ray post–flare loop ($\leq 20''$) indicates that the radio flux density observed with the shortest baseline of BIMA should be close to the total flux of the radio source. We have used the ratio of the intensities observed by SXT with the Al.1 and AlMg filters to determine the temperature of the post-flare loop at 23:22 UT during the gradual decay phase of the event. We find $T_e = 5.6 \pm 0.4 \times 10^6$ K, in agreement with GOES result.

2.2.2. Hard X-ray Observations

This small event was detected in hard X–rays by the CGRO-BATSE instrument. Figure 1 shows the time history of the flare in hard X-rays (LAD/CONT data, 20 – 169 keV). Like all the microwave frequencies, the hard X–rays peak during the impulsive spike at 23:04 UT (the "hard X–ray phase"). However, the X–rays decay rapidly after this peak and there is no detectable hard X–ray feature corresponding to the subsequent millimeter phase peaking at 23:05 UT and lasting until 23:08 UT. There is no obvious delay between the onset of the hard X-rays and the 17 GHz emission to within the 2 second resolution of the CONT data, although the 17 GHz peak is delayed relative to the hard X–ray peak. The onset of millimeter emission during the hard X–ray phase does appear to be delayed with respect to the emission detected at other wavelengths. In order to determine this delay, we have determined onset times using a linear fit to the initial steep rise in the lightcurve extrapolated to the mean preflare flux level, for each of the wavelengths. From these fits we find that the 86 GHz emission onset is delayed by 7 $\pm$ 2 s with respect to the 25 - 50 keV time profile.

There are sufficient hard X–rays for us to measure the energy spectral index of the X–ray–emitting electrons using the BATSE LAD/CONT data. We assume that the energy distribution of the hard X-ray photons is a simple power-law of the form:

$$I(E) = A_1 \left(\frac{E}{50\ \mathrm{keV}}\right)^{-\gamma} \tag{2}$$

where E is the photon energy (keV), I is the hard X-ray count rate (photons $\mathrm{s}^{-1}\ \mathrm{cm}^{-2}\ \mathrm{keV}^{-1}$), and γ the photon spectral index. Here γ and A_1 represent the fitting parameters. The resulting photon spectrum fitted to the CONT data between 23:03:41 and 23:04:12 UT in the energy range 29 - 126 keV is shown in Figure 6. Using the SPEX analysis program of R. Schwartz to carry out background subtraction, calculate response matrices and fit the spectrum, we find $\gamma = 3.4$ and $A_1 = 6.5 \times 10^{-3}$, corresponding to a thick–target electron energy spectral index of $\delta = \gamma + 1.5 \sim 4.9$, which is a typical value for flares (e.g., Dennis 1985). There are insufficient counts above 100 keV for any conclusions regarding the possible presence of a spectral break at higher energies to be drawn.

3. DISCUSSION

The flare discussed in this paper is a simple, small flare without reported associated Hα flare emission. Its thermal counterpart as measured by the GOES detectors is of class B5.6. The duration and the hard X-ray and radio time profiles suggest that the event is an impulsive flare in the classification of Kosugi et al. (1988). Despite its small importance, this event was detected in the impulsive phase at millimeter wavelengths, implying the presence of high-energy (≥ 1 MeV) electrons. This event thus reinforces the observation that flares of all sizes are capable of accelerating electrons to MeV energies, noted by Kundu et al. (1990), Lim et al. (1992), and Kundu et al. (1994).

3.1. Nonthermal emission during the impulsive phase of the flare

The radio spectra clearly indicate that the millimeter emission during both the hard X–ray and millimeter phases was nonthermal. We can rule out the possibility that a significant fraction of the radio emission detected during the impulsive phase is due to thermal free-free emission from a hot ($7\ \times 10^6$ K) plasma since the radio spectra clearly are not thermal, and the GOES fluxes during the impulsive phase are too weak to be consistent with such strong thermal radio emission. Because plasma emission does not play any significant role in solar radio emission above 10 GHz, the only suitable mechanism for nonthermal millimeter emission is gyrosynchrotron emission in coronal magnetic fields (White & Kundu 1992).

We now derive approximate physical parameters of the radio source at the time of the peak of the hard X–ray phase assuming that the emission is gyrosynchrotron emission from a single homogeneous source. The optically–thin radio spectrum then depends only on the total number of nonthermal electrons in the source, their energy spectral index, the magnetic field strength, and the angle between the magnetic field and the line of sight. We do not have sufficient data to determine all four parameters, and we will not carry out a complete parameter search here because the results are not of great interest and would not add to our physical understanding of this event. Instead, we will initially adopt the most straightforward parameters for the magnetic field magnitude and direction and source volume based on the observations and use them to derive the spectral index and number density of electrons. Subsequently we will discuss ways in which the parameters of the radio source can and need to be modified to remain consistent with the X–ray data.

We assume that the radio source is located at the top of the loop: since the soft X-ray post-flare loop is oriented along the solar north-south direction and the loop is close to the solar equator, we can assume that the angle between the line of sight and the magnetic field in the loop is large: we choose $\theta = 80°$. The relatively weak polarization seen in the 17 GHz maps is consistent with a large value for θ. Since ν_{peak} has been well determined by OVRO to be 6 – 7 GHz, the 17 GHz and 86 GHz radio emissions are optically thin. Further, ν_{peak} fixes the magnetic field to be $\sim$ 300 G, for typical values of the coronal density (Dulk & Marsh 1982). The upper limit to the longitudinal photospheric magnetic field strength in the vicinity of the flare loop is 400 G based on the Kitt Peak magnetogram, but since the flare is at S12W39 the total field strength may be larger than this, so the assumed coronal field is below the likely maximum photospheric field strength. We use an accurate homogeneous gyrosynchrotron code to fit the 17 and 86 GHz data points: once B and the source size are assumed, the density N and energy spectral index δ_r can be determined uniquely. Assuming a source area of 4×10^{17} cm^2 (linear dimension of $\sim 6'' \times 13''$, roughly consistent with the BIMA images) and line–of–sight depth of 4×10^8 cm, we find that the radio spectrum from 17 to 86 GHz at the time of the microwave peak (23:04 UT, 28 and 1.6 sfu at 17 and 86 GHz, respectively) requires a nonthermal electron number density of $N_0 = (1.3 \pm 0.1) \times 10^7$ cm^{-3}, where N_0 is the nonthermal density of electrons above 20 keV, with an energy spectral index of 3.6 ± 0.1 (slightly steeper than the rough estimate made earlier, since at 86 GHz the harmonic number is $\sim$ 100, and the Dulk and Marsh approximations are no longer accurate at such high harmonics where the emitted spectrum flattens towards the synchrotron limit, $\delta = 1 - 2\alpha$). The source dimensions assumed in this calculation are somewhat uncertain, but the main effect of a change in the volume of the loop is to change the trapping time for the electrons and this will be discussed in the following section. The spectrum predicted for the model source is plotted as a thick dashed line on Fig. 4. The fit is surprisingly good at low frequencies, given that we did not use any low–frequency data in the fitting procedure. However, the fit is poor in the vicinity of the spectral peak where the model fluxes are much larger than those observed. We also considered inhomogeneous dipole–loop models for the radio spectrum, but these did not solve the problem that the predicted spectral peak is much sharper than observed, and did not change the conclusions significantly. Because they involve more free parameters than homogeneous models, we will not discuss such models in detail here.

To conclude this section, we reaffirm the need for MeV–energy electrons to explain the high–frequency emission. For the parameters derived above we assumed a power–law electron energy distribution from 20 keV to 20 MeV. If we use the same power law index but place the high–energy cutoff at 500 keV (i.e., keep all the electrons likely to emit hard X–rays below 150 keV), then the 9.5 GHz flux drops to 53% of its previous level, the 17 GHz flux drops to 14% of its previous level, and the 86 GHz flux is too small for the code to calculate (a drop of at least 7 orders of magnitude). Thus any nonthermal millimeter emission in the impulsive phase does indeed require the presence of MeV–energy electrons.

3.2. The energy spectrum of the radiating electrons

In this section we attempt to reconcile the hard X–ray and radio spectra during the hard X–ray phase. We do so by calculating the electron energy distribution per unit volume for each electron population. There are two general classes of model for the hard X–ray emission from solar flares. In the "thin–target" model, the nonthermal electrons are very effectively trapped in the corona and produce hard X–rays via bremsstrahlung on the ambient coronal ions: in that case the hard X-ray photon spectral index γ is related to the electron energy spectral index δ_x by $\delta_{x,thin} = \gamma - 0.5$. In the "thick–target" model, the nonthermal electrons are trapped in closed magnetic loops where the ambient density is sufficiently low that collisions are ineffective in changing the electron energies. In this case the bulk of the hard X–rays are produced via bremsstrahlung when the nonthermal electrons strike the dense chromospheric material at the footpoints of the coronal loop, and $\delta_{x,thick} = \gamma + 1.5$.

We convert the photon spectrum of $I(E_\nu) = A\,E_\nu^\gamma$ photons cm^{-2} s^{-1} keV^{-1}, where $\gamma = 3.43$ and $A = 6.0 \times 10^3$ (at the time of the hard X–ray peak; we have scaled the rate derived earlier by the ratio of the peak count rate to the mean count rate during the interval over which the spectrum was measured), to the corresponding power–law energy spectrum of the radiating electrons in the thick–target and thin–target limits, respectively, following the prescription of Hudson et al. (1978) and Nitta et al. (1991):

$$(\frac{dN(E)}{dE})_{thick} = \frac{2.48\times10^{24}}{S_{thick}}\,b(\gamma)\,A\,E^{-(\gamma+1.5)} = \frac{1.63\times10^{29}}{S_{thick}}\,E^{-4.93} \quad \text{electrons cm}^{-3}\ \text{keV}^{-1} \tag{3}$$

$$(\frac{dN(E)}{dE})_{thin} = \frac{1.05\times10^{42}}{N_i\,V_{thin}}\,c(\gamma)\,A\,E^{-(\gamma-0.5)} = \frac{1.28\times10^{46}}{N_i V_{thin}}E^{-2.93} \quad \text{electrons cm}^{-3}\ \text{keV}^{-1} \tag{4}$$

For the thin–target model, we have divided the total number of electrons by the volume of the loop, V_{thin}, in order to convert to volume density. For the thick–target model, we have converted the differential electron flux $dF(E)/dE$ (electrons keV^{-1} s^{-1}) into the corresponding differential electron density distribution in the coronal loop using $dF(E)/dE = S_{thick}\ v_z\ dN(E)/dE$, where S_{thick} is the area of the thick target (i.e., the area of the loop footpoint at the chromosphere) and v_z is the mean downwards velocity of electrons at the footpoint, here taken arbitrarily to be $v/\sqrt{2}$ (in the absence of detailed knowledge of the pitch–angle distribution). This is equivalent to defining the lifetime of an electron in the loop to be $\tau = V_{thin}/v_z S_{thick}$, and assuming that the hard X–ray emitting electrons are in the strong pitch–angle scattering regime. We discuss the effects of relaxing this assumption below. The parameters $b(\gamma)$ and $c(\gamma)$ are multipliers of order 10 and 1, respectively (see Hudson et al. 1978).

We do not have hard X-ray imaging observations which can be used to constrain the choice of thin or thick-target model, e.g., by showing footpoints in hard X–rays corresponding to the flare loop seen in soft X–rays, so we will proceed by assuming that the post–flare loop is essentially the flare loop. This loop has a length $\sim\ 1\ \times\ 10^9$ cm and a diameter $\sim\ 4\ \times\ 10^8$ cm at the footpoints, i.e., $S_{thick}\ \sim\ 1\ \times 10^{17}$ cm^2 (assuming a cylindrical cross–section; this area is typical of hard X–ray footpoints: e.g., Kosugi 1994) and $V_{thin} = 1\ \times\ 10^{26}$ cm^3, which is consistent with the radio source size inferred from the BIMA data. With these parameters, we find:

$$(\frac{dN(E)}{dE})_{thick} \sim \frac{6\times10^5}{S_{17}}\ (\frac{E}{20\ \mathrm{keV}})^{-4.9} \qquad \mathrm{electrons\ cm^{-3}\ keV^{-1}} \tag{5}$$

$$(\frac{dN(E)}{dE})_{thin} \sim \frac{2\times10^6}{N_{10}}\ (\frac{E}{20\ \mathrm{keV}})^{-2.9} \qquad \mathrm{electrons\ cm^{-3}\ keV^{-1}} \tag{6}$$

where S_{17} is the footpoint area in units of 10^{17} cm^2 and N_{10} is the ion density in units of 10^{10} cm^{-3}. Note that, as is generally the case, the thin–target model requires a much larger amount of energy to be carried by electrons above 20 keV than does the thick–target assumption. Earlier, from a careful fit to the 17 and 86 GHz fluxes at the time of the microwave and hard X–ray peak, we found that the nonthermal electrons radiating the high–frequency radio emission could be described by the energy distribution

$$\frac{dN_r(E)}{dE} = 1.3\times10^7\ (\frac{E}{20\ \mathrm{keV}})^{-3.6} \qquad \mathrm{electrons\ cm^{-3}\ keV^{-1}} \tag{7}$$

The spectral index in this expression is steeper than that of the thin–target result (6), but much flatter than that of the thick–target result (5).

The thin–target solution (6) can be ruled out since it is inconsistent with the high–frequency radio spectrum: such an energy distribution would dominate the radio emission (since it contains many more MeV–energy electrons than does (7)) and produce a radio spectrum flatter than we observe. Therefore, in common with most flares, we assume that the hard X–rays are dominated by emission from thick–target sources, and therefore there is a discrepancy between the power–law indices of the electron energy distributions in the hard X–ray–emitting ($\leq$ 200 keV) and millimeter–emitting ($\geq$ 1 MeV) domains, as has often been found previously (e.g., Kundu et al. 1994). However, the number densities derived in (5) and (7) still represent an embarrassment for this interpretation, since for the assumed values of magnetic field B = 300 G, angle θ = 80° and footpoint area S_{thick} = 10^{17} cm^2, there are more electrons in the spectrum of radio–emitting electrons than in the X–ray–emitting spectrum at all energies above 20 keV, and this is clearly inconsistent with the assumption that $\geq$ 20 keV hard X–rays from the radio–emitting electrons are not detected.

We are thus faced with a contradiction which does not arise when the electron distribution derived from the radio data contains fewer hard X–ray–emitting electrons than the electron distribution derived from the hard X–ray spectrum. We will therefore investigate whether we can modify the parameters of the two sources to reconcile the two distributions, while still remaining consistent with the available observations. In order for the thick–target energy distribution to dominate the observed hard X–rays below 100 keV, we require that their number density exceed that of the radio–emitting electrons below about 300 keV. We based the earlier value for S_{thick} on the *coronal* cross–section of the flaring loop, but the actual size of the footpoint area can be much smaller if the loop tapers considerably at its footpoints, so we will now assume S_{17} = 0.1 in (5). (Since smaller footpoints mean a smaller loss cone in the loop, note that strongly tapering the loop at the footpoints will have the effect of increasing trapping times compared to an untapered loop.) A decrease in θ would lower the opacity and require an even larger value for the number density of radio–emitting electrons, so we will continue to assume that θ = 80°. Since the optically–thin gyrosynchrotron flux is roughly proportional to $N_e B^{0.9\delta_r - 0.2} \approx N_e B^3$, an increase in B can dramatically lower the number of radio–emitting electrons required, but at the expense of an increase in the frequency of the spectral peak which is not consistent with the OVRO spectra: with B = 500 G we can fit the 17 and 86 GHz data with the same geometry as previously, but now with 1.5×10^6 $(E/20\,\mathrm{keV})^{-3.4}$ electrons cm^{-3} keV^{-1}, while if B = 800 G we can fit the 17 and 86 GHz data with 2×10^5 $(E/20\,\mathrm{keV})^{-3.2}$ electrons cm^{-3} keV^{-1}. The two corresponding radio spectra are also shown on Fig. 4, as thin dashed and thick dotted lines, respectively: in contrast to the 300 G model which is quite smooth on the low–frequency side of the spectral peak, the two higher–B models show considerable harmonic structure at low frequencies which the OVRO data do not exhibit. However, harmonic structure such as this may be smoothed out in a more realistic source in which a small spread of magnetic fields produces overlapping harmonics which, when summed, give a much smoother low–frequency spectrum while changing the high–frequency spectrum only slightly.

If we now take the hard X–ray thick–target electron spectrum with small footpoints,

$$(\frac{dN(E)}{dE})_{thick} \sim \ 6 \times 10^6 \ (\frac{E}{20 \text{ keV}})^{-4.9} \qquad \text{electrons cm}^{-3} \text{ keV}^{-1} \tag{8}$$

and the B = 800 G electron energy spectrum inferred from the radio data,

$$(\frac{dN_r(E)}{dE}) = 2 \times 10^5 \ (\frac{E}{20 \text{ keV}})^{-3.2} \qquad \text{electrons cm}^{-3} \text{ keV}^{-1} \tag{9}$$

then the X–ray emitting population exceeds the radio–emitting population at all energies below about 220 keV. Thus if we make S_{thick} small and allow a large B we can find a self–consistent combination of parameters in which the X–ray emitting and high–frequency–radio–emitting electrons are distinct populations. However, the radio data in the vicinity of the spectral peak are not fit by the 500 and 800 G models any better than they are by the 300 G model. Note that the 17 GHz flux produced by the X–ray–emitting electrons (8) in, e.g., a B = 500 G model is only 2 sfu, whereas at B = 800 G the 17 GHz flux would be around 25 sfu (the 86 GHz flux from the steep–spectrum electrons is negligible in both cases). Thus using a very high magnetic field strength means that the lower–energy steep–spectrum electrons can contribute significantly at microwave frequencies. This in turn diminishes the 17 GHz flux attributed to the millimeter–emitting electrons and implies a harder distribution for them, with a smaller number density, which helps to reconcile the X–ray and radio data.

Spectral hardening at high energies similar to that inferred here has been observed previously in X-ray/γ-ray/microwave data sets (Dennis 1988, Vilmer 1997). However those observations refer to large flares, unlike the event presented in this paper (GOES class B5.6). In other studies including small flares, it has been inferred that the high-energy electron distribution differs from the low-energy distribution (Alissandrakis 1986, Staehli, Gary & Hurford 1989, Lim et al. 1992, Kundu et al. 1994, Silva et al. 1997). In some previous studies there had been ambiguity regarding the radio spectral index because of uncertainty in the spectral peak frequency: in this paper, as in Silva et al. (1996), the use of OVRO data allows us to determine the turnover frequency ν_{peak} unambigously, and its value of 6.5 GHz (typical for small flares) ensures that the 17 GHz and the 86 GHz emissions are optically thin, and they are then directly related to the energy distribution of the energetic emitting electrons. For this reason we are confident of our finding that the electron spectral indices derived from hard X-ray and radio data are different.

3.3. Relation between hard X-ray, microwave and millimeter time profiles

Figures 1 and 3 may be used to compare the time profiles of the flare at different wavelengths. There are two striking features of this comparison: hard X–rays are detected at a significant level only during the initial impulsive spike at 23:04 UT which dominates the microwave emission; and the microwave and millimeter peaks represent two quite distinct components. No significant hard X–rays are detected during the nonthermal millimeter phase from 23:04:20 to 23:08 UT.

This behaviour can be understood in a simple trap model if there are two separate injections of accelerated electrons. Since electrons will radiate millimeter emission as long as they reside in the strong magnetic fields of the corona, but (in the thick target model) produce X–rays only once, when they precipitate, the ratio per electron of radio flux to hard X–ray flux is proportional to the typical trapping time of the electrons in the corona (equivalently, the ratio of the number density in the corona to the rate of precipitation is proportional to the trapping time; e.g., Hudson & Ohki 1972, Takakura 1972, Gary 1985, Lu & Petrosian 1989). Therefore we require that the energetic electron component injected during the hard X–ray phase has a very short trapping time and a relatively soft spectrum. The electron energy distribution injected during the millimeter phase has a much longer trapping time and a harder spectrum. The difference in the energy spectra follows immediately from the change in the high–frequency spectral index of the radio emission, which hardens by ~ 0.8 between 23:04 UT (upper curve in Fig. 4) and 23:05 UT (middle curve in Fig. 4). The initial injection of hard X–ray emitting electrons peaking at 23:04 UT produced relatively little millimeter emission but quite strong microwave emission. The subsequent large ratio of millimeter emission to microwaves during the millimeter phase is due to the harder electron distribution. However, the absence of significant hard X–rays at this time cannot be explained just by the harder spectrum. Instead, we suggest that the total number of electrons injected during the millimeter phase is small, but if they have a much longer trapping time in the corona then the small number of electrons explains why they produce little bremsstrahlung hard X–ray emission; but they continue to radiate microwave and millimeter emission as long as they remain trapped in the corona. For a radio source of the same physical dimensions used during the hard X–ray phase and a magnetic field of 800 G, we find that the 17 GHz flux (16 sfu) and 86 GHz flux (3.2 sfu) at the peak of the millimeter phase can be explained by a spectrum of the form

$$(\frac{dN_r(E)}{dE}) = 1 \times 10^4 \ (\frac{E}{20 \text{ keV}})^{-2.3} \qquad \text{electrons cm}^{-3} \text{ keV}^{-1} \tag{10}$$

and on converting this to 20–170 keV hard X–ray flux we find that even for a relatively large footpoint area of 10^{17} cm^2 (i.e., a relatively short trapping time) the flux detected by a BATSE detector would be only several counts per second and therefore not distinguishable from noise. If we assume a smaller magnetic field then the number of electrons required is larger. In order for the X–rays from the larger number of nonthermal electrons to remain undetected, their trapping time needs to be longer, meaning that the ratio of the footpoint area to the looptop cross section must be smaller (a smaller loss cone requires a larger ratio of B at the footpoint to B at the looptop).

There does need to be a separate injection of electrons to explain the millimeter phase, since the number of MeV–energy electrons present in the corona clearly must be increasing from 23:04 to 23:05 UT in order for the optically–thin radio flux at 17 and 86 GHz to be increasing during this time, and this increase cannot be achieved simply by a change in the energy distribution such as removing the low–energy electrons. Further, since the millimeter emission during the hard X–ray phase decays as rapidly as the hard X–rays and microwaves, the trapping time in the hard X–ray phase of the event must be short for all energies. This is not consistent with collisional scattering, which causes lower–energy electrons to have much shorter trapping times than MeV–energy electrons. Whether the longer trapping time during the millimeter phase is due to the electrons having been injected with a different pitch–angle distribution, or whether the electrons are in a loop with a larger mirror ratio than the hard X–ray emitting electrons which will also produce longer trapping times, cannot be determined from these data. However, the smooth time profile observed during the millimeter phase argues that pitch–angle scattering of these trapped electrons is weak: for strong scattering the lifetime is the loop crossing time times the ratio of B at the footpoint to B at the looptop (Melrose & White 1979), and for the parameters of this source (loop length 10^9 cm, crossing time 0.06 seconds at $0.5c$) strong scattering cannot produce a decay time of order 60 s unless this magnetic field ratio is of order 1000, which seems implausible.

We note that the ambient coronal density on field lines where the hard X–ray phase occurred is likely to be increasing during the millimeter phase, since the GOES time profile shows a steady increase in soft X–ray emission. Such an increase in density implies that the trapping time due to collisions should be *shorter* during the millimeter phase than during the hard X–ray phase on those field lines. If the difference in trapping times between the hard X–ray and millimeter phases is due to the electrons being in a different loop, the imaging data should show this. We do not measure different positions for the different millimeter components in this flare (Fig. 5) at the level of several arcseconds, implying that the two components probably are in the same loop. Unfortunately, having data from just 4 antennas, combined with poor atmospheric phases during the observations, means that we cannot reliably determine positional shifts smaller than several arcseconds for these data, and so the data could still be consistent with two distinct but very small loops being involved.

The decay of the radio emission in the millimeter phase after 23:05 UT can be due to collisional energy loss of the electrons, which should be accompanied by a hardening of the spectrum as the low–energy electrons lose energy faster; or to the loss of electrons from the corona by precipitation after they are scattered into the loss cone. The OVRO radio spectra show a slight increase in peak frequency (from 7 to $\sim$ 8 GHz) with time, but the microwave fluxes are generally too weak during the decay of the trapped component to determine whether significant hardening is occurring. The inferred e–folding decay time from the data during the millimeter phase is of order 1 minute. The decay time for collisional energy loss by relativistic electrons is $2.6 \times 10^9\ E_{keV}/N_i$ (Trubnikov 1965), which is of order 60 s at 1 MeV for a coronal density of $N_i = 5 \times 10^{10}$ cm^{-3}. The decay time due to precipitation at energy E from collisions in the weak–diffusion limit is roughly the angular scattering time (in the limit that this is longer than the loop crossing time for the electrons), which is half the energy decay time (Trubnikov 1965, Melrose & Brown 1976). Thus collisional scattering of large pitch–angle electrons into the loss cone provides a plausible explanation for the decay timescale during the millimeter phase.

We note that the onset of millimeter emission was delayed by 8 seconds compared to the other observed wavelengths. Similar delays of the millimeter emission have already been noted previously (Lim et al. 1992, Kundu et al. 1994). Among roughly 15 events studied, the impulsive millimeter emission has never been observed to precede the microwaves and hard X-rays. For those events with enough signal-to-noise ratio, the delays were in the range 5 - 10 s. The travel time of high pitch angle and high energy electrons may exceed that of low pitch angle, low energy electrons. However this effect has been studied by Lu and Petrosian (1990), and the delays derived do not seem to exceed 1 s. Alternatively, as suggested by Lim et al. (1992) and Kundu et al. (1994), the delay may indicate that high energy electrons are accelerated later than the lower energy electrons responsible for hard X-ray/microwave emission, as originally suggested by Bai & Ramaty (1976, 1979). More detailed studies of such delays are necessary to know whether during the impulsive phase of an eruption one or two acceleration mechanisms are at work.

3.4. Thermal bremsstrahlung emission during the gradual phase of the flare

During the gradual phase the observed flux is independent of frequency. This suggests that, as expected, the emission is due to optically–thin thermal bremsstrahlung. Using the emission measure EM and temperature T_e derived from GOES measurements (which agree with the SXT data during the period of overlap), we can deduce the temporal evolution of the predicted flux at 86 GHz and compare with the observed flux. This was done in Fig. 2d: the agreement is excellent both in time profile and in flux magnitude, given the uncertainty in the BIMA calibration. Note that the peak of the radio flux predicted from the GOES data is much later than the peak in the GOES 1 – 8 Å flux profile of Fig. 2c, being closer to the peak of the GOES emission measure profile: this is because at soft X–ray wavelengths the combined bremsstrahlung and line emission flux is a sensitive function of temperature, whereas the radio flux is only weakly sensitive to temperature and therefore more closely follows the behaviour of the emission measure.

4. CONCLUSIONS

In this paper we have reported on the observation of a small (GOES class B5.6), compact flare, detected in X-rays, microwaves and at millimeter wavelengths. At radio wavelengths the flare shows three clearly separate phases: a “hard X–ray” phase of roughly 1 minute during which hard X–rays and microwaves are strong; additional nonthermal radio emission lasting three minutes during which there were no detectable hard X–rays, and the millimeter emission was relatively strong (the “millimeter” phase); and a longer–duration gradual decay which lasted for roughly 30 minutes. The latter phase is identified with thermal emission from a < 6 MK plasma. The simultaneous availability of radio spectra and imaging allow many of the parameters of the flare radio source to be determined. During the hard X–ray phase the radio–emitting electrons had a spectral index of -3.6, while the hard X–ray emitting electrons had a spectral index of -4.9 for thick–target emission. During the subsequent millimeter phase, the spectral index of the radio–emitting electron energy distribution was significantly harder.

Energy distributions for the hard–X–ray–emitting electrons and for the millimeter–emitting electrons during the hard X–ray phase of the impulsive emission can be derived from the hard X–ray and high–frequency radio spectra, respectively, using plausible physical parameters (source dimensions, magnetic field strength) based on observations. However, the simplest assumptions lead to a contradiction: the millimeter–emitting electrons are so numerous that their thick–target bremsstrahlung emission should dominate the hard X–rays and produce a spectral index consistent with the radio spectral index. This is not observed. In order quantitatively to reconcile the hard X–ray and radio data with two distinct populations, we would require that the magnetic field in the loop be much stronger than would be expected either based on the photospheric fields in the vicinity, or from the location of the microwave spectral peak; and we further require that the flare loop taper considerably at the chromosphere (footpoint area $\ll$ coronal cross section). These assumptions are not justified by the available data, and the resulting model does not fit the radio spectra satisfactorily.

We postulate that the two distinct periods in the impulsive phase differ in the physical characteristics of the source: during the hard X–ray phase nonthermal electrons were more numerous, but precipitated rapidly out of the corona. During the subsequent millimeter phase when hard X–rays were not observed, we argue that the radiating electrons were few, but remained in the corona for a much longer period. Their bremsstrahlung hard X–rays were spread over a long time and therefore were not detected above the noise level. The reason for this difference in trapping times is not understood: if the radio source occupies the same field lines for both impulsive components and if wave scattering is the predominant mechanism for pitch–angle scattering, the increase in trapping time could be due to a decrease in the level of wave turbulence in the corona. Alternatively the different trapping times can be explained if the two sources occupy different field lines (also suggested by the results of Hanaoka 1997 and Nishio et al. 1997), and in the millimeter phase the source lies on field lines with a larger mirror ratio which will naturally produce a longer trapping time.

The occurrence of a phase during which MeV electrons were clearly present in the corona while there was no detectable evidence for lower–energy hard X–ray emitting electrons is unusual: in most previous millimeter studies of flares any nonthermal millimeter emission, indicating the presence of MeV–energy electrons, has occurred during the period of detectable hard X–ray emission (Kundu et al. 1994, Silva et al. 1997). However, calculations show that such a situation is entirely consistent with trap models *provided* that the millimeter–emitting electrons have a relatively flat energy distribution. We emphasize that, independently of the comparison of the radio and hard X–ray spectra, the radio data alone require different energy spectra to be present during the hard X–ray and millimeter phases, respectively, and therefore two episodes of acceleration are apparently required to explain this event.

Finally we would like to note that we could not fully exploit the spatial imaging capabilities of BIMA for the 1994 August events because only 4 of the antennas were available while the Sun was in a flaring state. At present BIMA consists of 10 antennas, and much improved solar flare images can be anticipated.

Solar radio research at the University of Maryland is supported by NASA under the GRO GI program (NAG–W–1540) and grant NAG–W–1541, and by the NSF under grant ATM 93–16972. The use of BIMA for scientific research at the University of Maryland is supported by NSF grant AST 93–14847. JPR received partial support from FAPESP (Proc. 9606956-1). This research has made use of data obtained through the CGRO BATSE Solar Flare Data Archive maintained by the Solar Data Analysis Center at NASA-Goddard Space Flight Center and provided by the BATSE team headed by Dr. Gerald Fishman. The soft x-ray images are from the Yohkoh mission of ISAS, Japan. The soft x-ray telescope was prepared by the Lockheed Palo Alto Research Laboratory, the National Astronomical Observatory of Japan, and the University of Tokyo with the support of NASA and ISAS. We thank the referee for his careful reading of the paper and detailed comments.

REFERENCES

Alissandrakis, C. E. 1986, Solar Phys., 104, 207.

Bai, T., & Ramaty, R. 1976, Solar Phys., 49, 343.

Bai, T., & Ramaty, R. 1979, ApJ, 227, 1072.

Dennis, B. R. 1985, Solar Phys., 100, 465.

Dennis, B. R. 1988, Solar Phys., 118, 49.

Dulk, G. A., & Marsh, K. A. 1982, ApJ, 259, 350.

Gary, D. E. 1985, ApJ, 297, 799.

Hanaoka, Y. 1997, Solar Phys., 173, 319.

Hudson, H. S., Canfield, R. C., & Kane, S. R. 1978, Solar Phys., 60, 137.

Hudson, H. S., & Ohki, K. 1972, Solar Phys., 23, 155.

Kosugi, T. 1994, in Proceedings of the Kofu Symposium on a New Look at the Sun, ed. S. Enome & T. Hirayama (Nobeyama: Nobeyama Radio Observatory), p. 11.

Kosugi, T., Dennis, B. R., & Kai, K. 1988, ApJ, 324, 1118.

Kundu, M. R. 1961, J. Geophys. Res., 66, 4308.

Kundu, M. R., White, S. M., Gopalswamy, N., Bieging, J. H., & Hurford, G. J. 1990, ApJL, 358, L69.

Kundu, M. R., White, S. M., Gopalswamy, N., & Lim, J. 1994, ApJS, 90, 599.

Lim, J., White, S. M., Kundu, M. R., & Gary, D. E. 1992, Solar Phys., 140, 343.

Lu, E. T., & Petrosian, V. 1989, ApJ, 338, 1122.

Lu, E. T., & Petrosian, V. 1990, ApJ, 354, 735.

Melrose, D. B., & Brown, J. C. 1976, MNRAS, 176, 15.

Melrose, D. B., & White, S. M. 1979, Proc. Astron. Soc. Aust., 3, 369.

Nitta, N., White, S. M., Schmahl, E. J., & Kundu, M. R. 1991, Solar Phys., 132, 125.

Silva, A. V. L., White, S. M., Lin, R. P., de Pater, I., Shibasaki, K., Hudson, H. S., & Kundu, M. R. 1996, ApJL, 458, L49.

Silva, A. V. L., Gary, D. E., White, S. M., Lin, R. P., & de Pater, I. 1997, Solar Phys., 175, 157.

Staehli, M., Gary, D. E., & Hurford, G. J. 1989, Solar Phys., 120, 351.

Takakura, T. 1972, Solar Phys., 26, 151.

Thomas, R. J., Starr, R., & Crannell, C.-J. 1985, Solar Phys., 95, 323.

Trubnikov, B. A. 1965, Rev. Plasma Phys., 1, 105.

Vilmer, N. 1997, in Coronal Physics from Radio and Space Observations (Lecture Notes in Physics **483**), ed. G. Trottet (Berlin: Springer), p. 28

Welch, W. J., & 35 others. 1996, PASP, 108, 93.

White, S. M., & Kundu, M. R. 1992, Solar Phys., 141, 347.

This preprint was prepared with the AAS LaTeX macros v4.0.

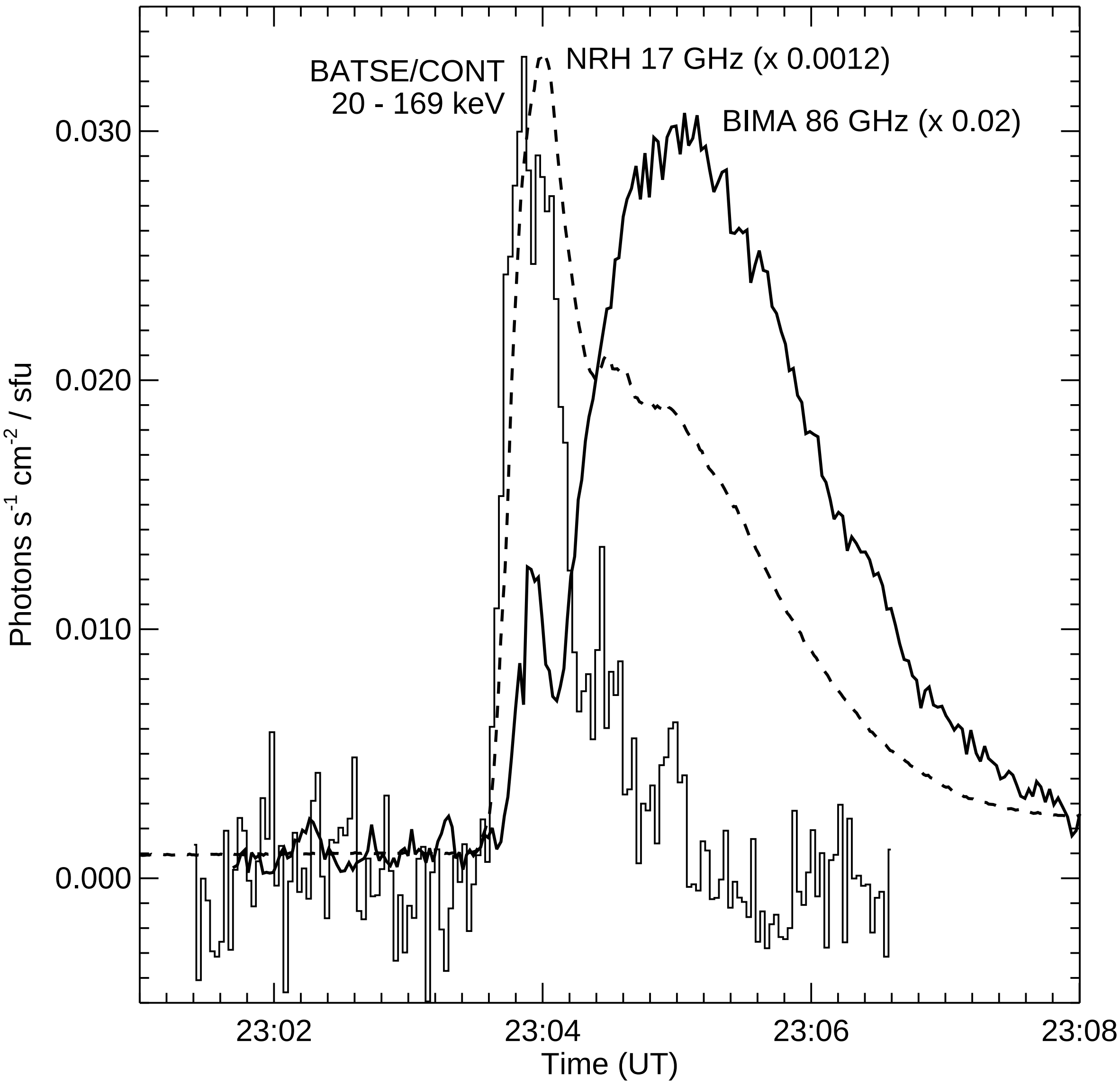

Fig. 1.— Detailed temporal evolution of the impulsive phase of the flare at hard X–ray (BATSE CONT data, 20 - 169 keV, 2 s time resolution), microwave (NRH 17 GHz, 1 s time resolution) and millimeter (BIMA 86 GHz, longest baseline, time resolution $\sim$ 1.7 seconds) wavelengths.

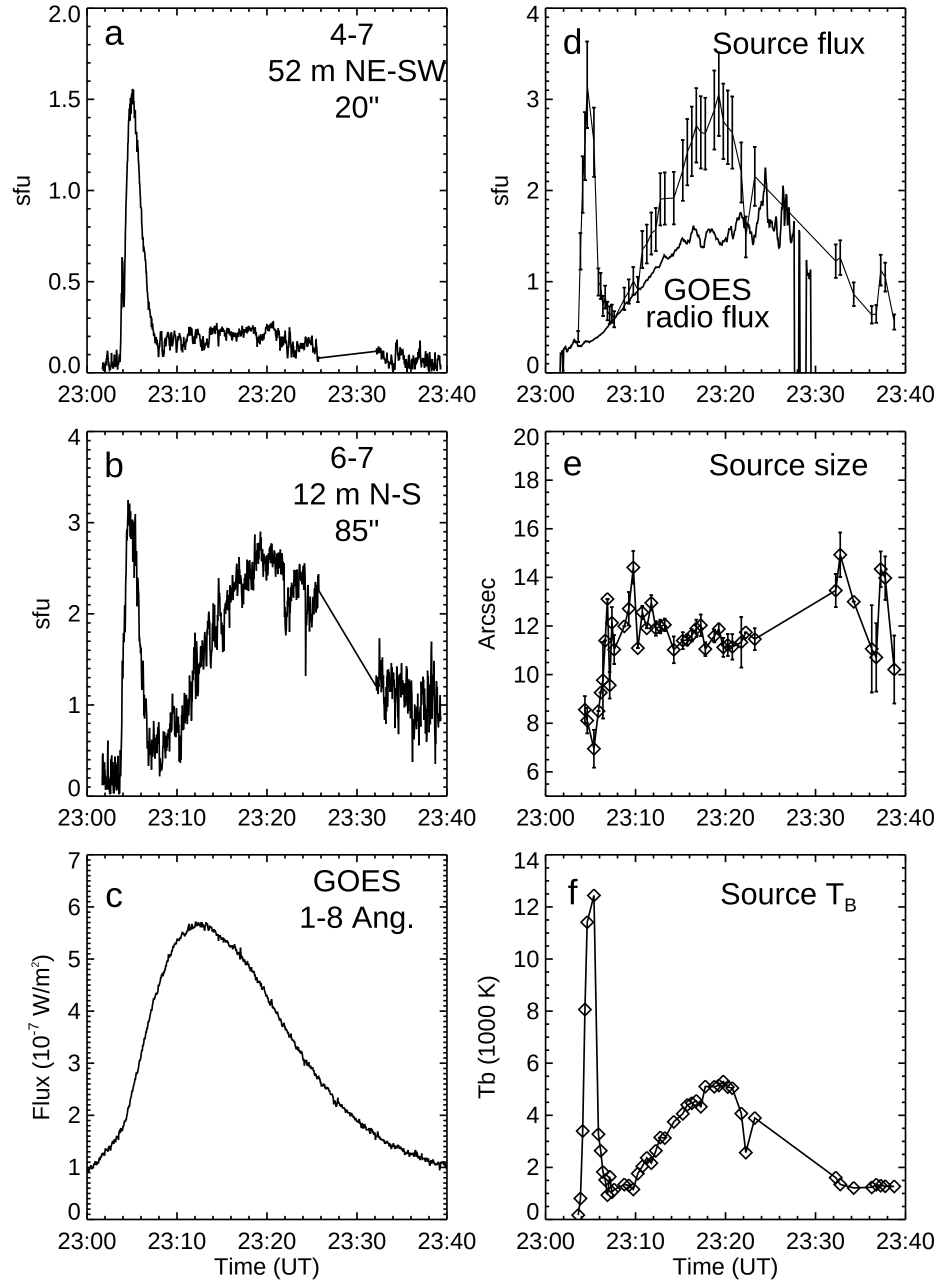

Fig. 2.— Figs. 2a,b show the temporal evolution of the radio flux densities observed at 86 GHz with BIMA baselines 4-7 (the longest baseline) and 6-7 (the shortest baseline), respectively. The length is indicated in each frame as well as the corresponding fringe spacing. Fig. 2c shows the time profile of the GOES 1–8 Å soft X–ray flux. 2d is the flux density of a gaussian model (points with error bars) which has been fitted to the BIMA data, together with the radio flux predicted from the free–free emission of the soft X–ray emitting plasma using temperatures and emission measures derived from the GOES data (thicker solid line). 2e is the fitted size of the corresponding gaussian source, and 2f shows the derived 86 GHz brightness temperature.

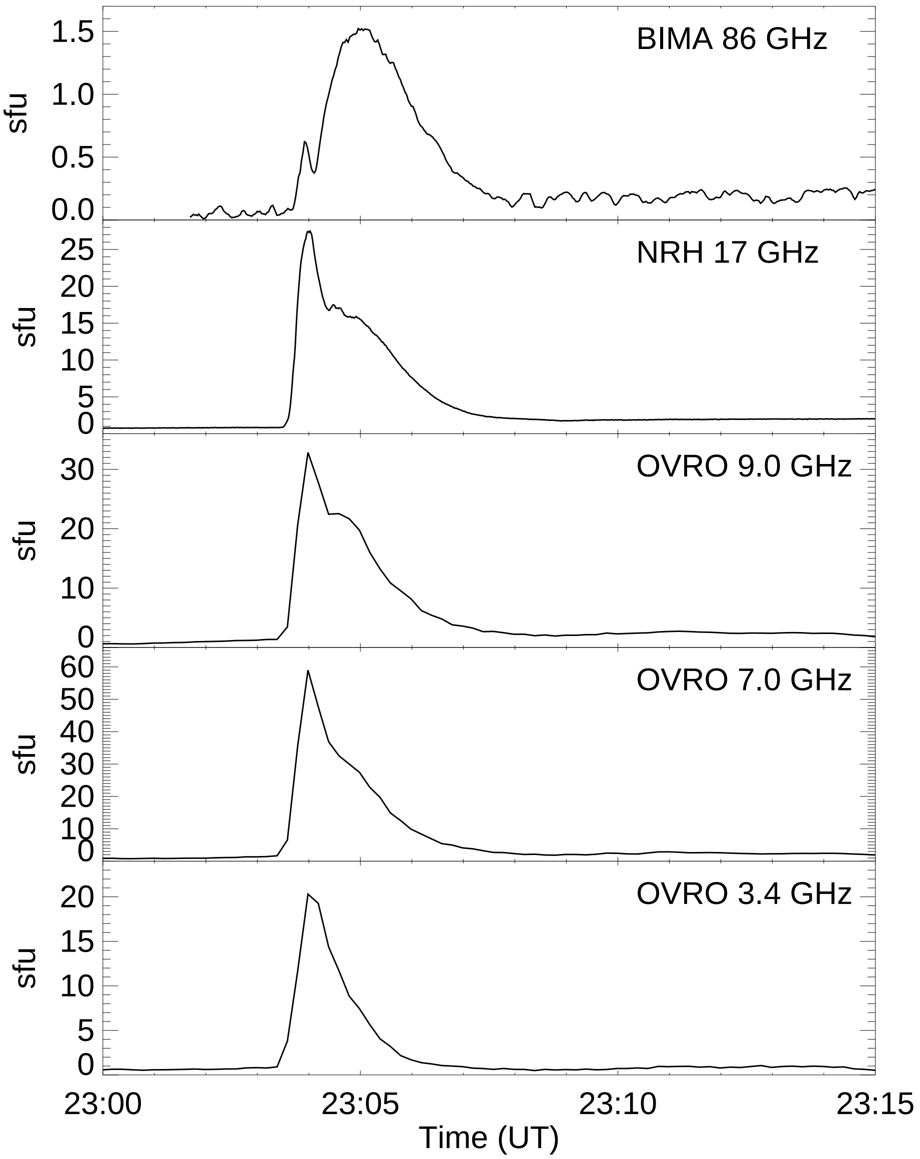

Fig. 3.— Comparison of time profiles observed by OVRO, BIMA and NRH during the impulsive phase and initial part of the gradual phase. The upper panel shows the BIMA 86 GHz flux measured on the longest baseline, in order to highlight the brief impulsive spike at 23:04 UT; note that the peak flux on shorter baselines is larger than shown here (see Fig. 2). The second panel shows 17 GHz data from NRH. These data are the "correlation coefficient" data which measure the flux in compact sources, scaled to match the flux in maps made at discrete times during the event from which the absolute flux can be determined. This comparison indicates that the "correlation coefficient" data provide a faithful representation of the flux evolution at 17 GHz for this event. The three lower panels show the correlated flux between the two 27 m antennas at OVRO at 9.0 (3rd panel), 7.0 (4th panel) and 3.4 GHz (bottom panel), at 12 second time resolution.

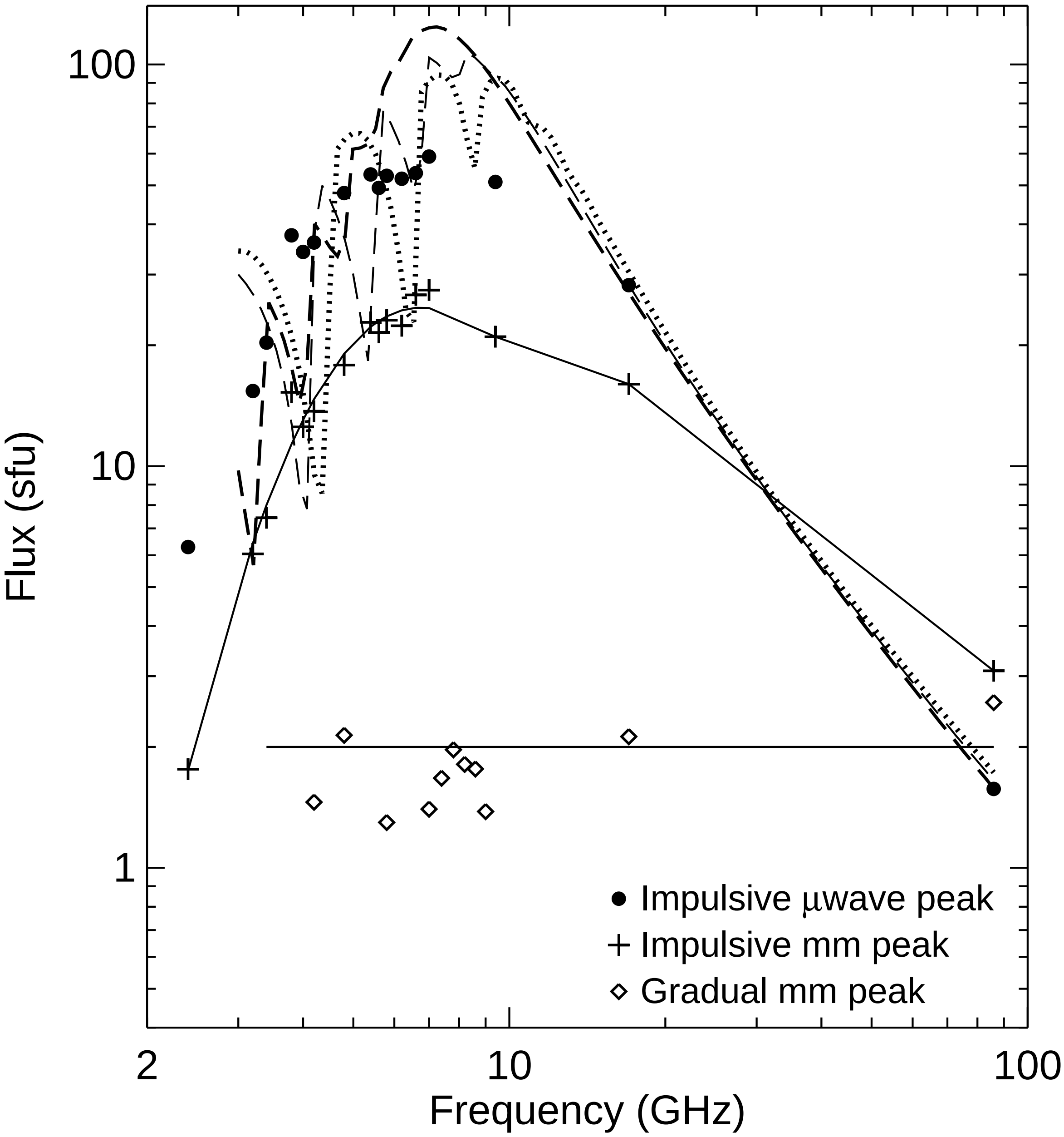

Fig. 4.— The radio spectrum at three different phases of the event: the peak of the impulsive microwave emission at 23:03:59 UT (filled circles), the peak of the impulsive millimeter emission at 23:04:59 UT (plus symbols), and the peak of the millimeter emission in the gradual phase (diamond symbols). The latter points are averages over 60 seconds centered at 23:17:59 UT. Data points below 8 GHz are OVRO total–power measurements; the 9.4 GHz points are from the Nobeyama polarimeter; the 17 GHz points are from the Nobeyama radoheliograph; and the 86 GHz points are from BIMA. The thick dashed curve is a homogeneous gyrosynchrotron model fit to the 17 and 86 GHz points at 23:04 UT using $B = 300$ G, as described in the text; the thin dashed curve is a fit for $B = 500$ G; and the thick dotted curve is a fit for $B = 800$ G. Thin solid lines to guide the eye (not fits) are drawn through the other two spectra.

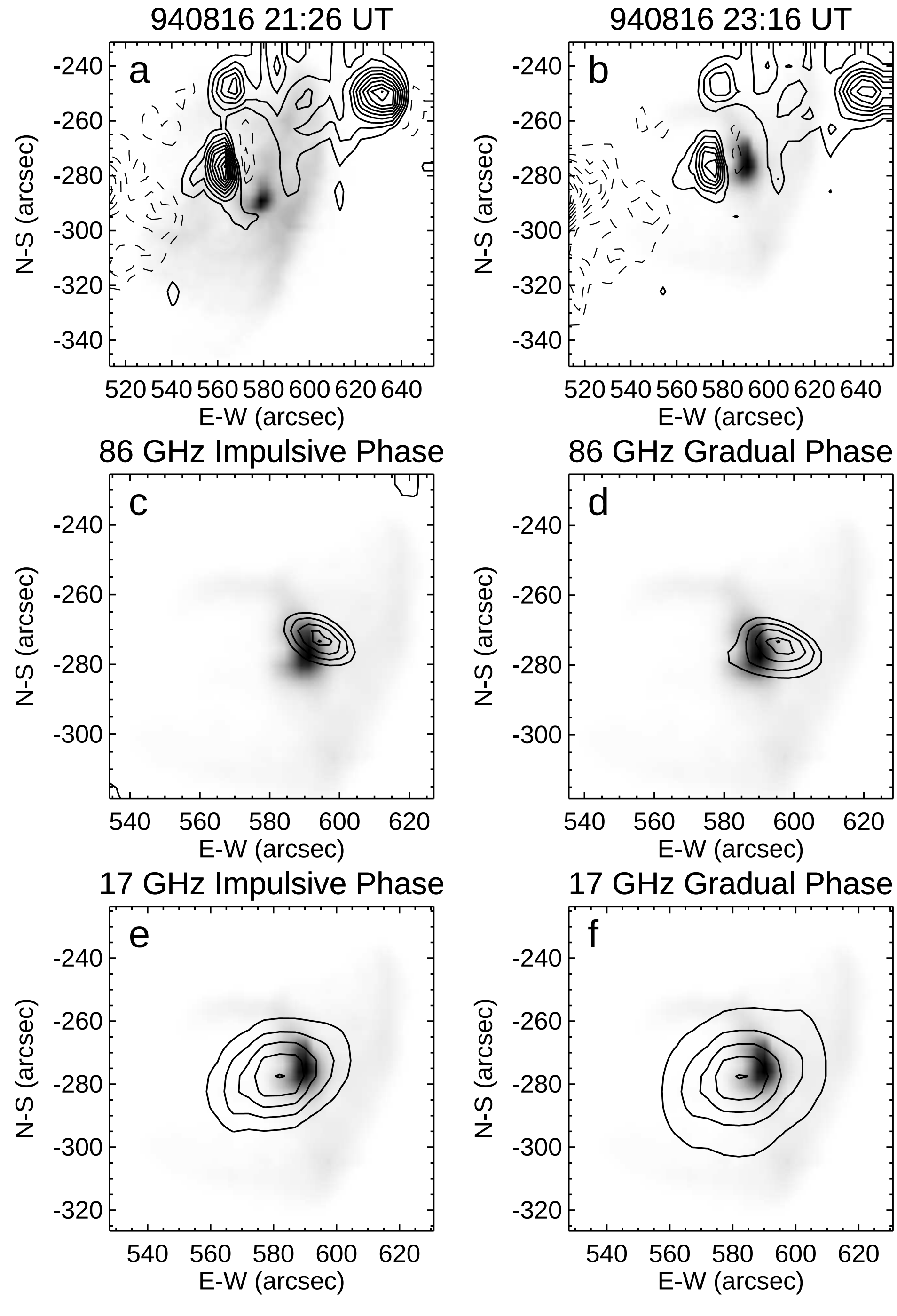

Fig. 5.— Panels (a) and (b) show soft X-ray pre-flare and post-flare images, respectively, on which contours of the longitudinal magnetic field have been superposed. The remaining panels all have the post–flare Yohkoh SXT soft X–ray image as a greyscale background, with contours of the the 86 GHz BIMA images of the impulsive phase (panel c) and gradual phase (panel d) and the Nobeyama radioheliograph 17 GHz images of the impulsive phase (panel e) and gradual phase (panel f) superposed. The differences in position between the 17 and 86 GHz radio sources are not believed to be significant.

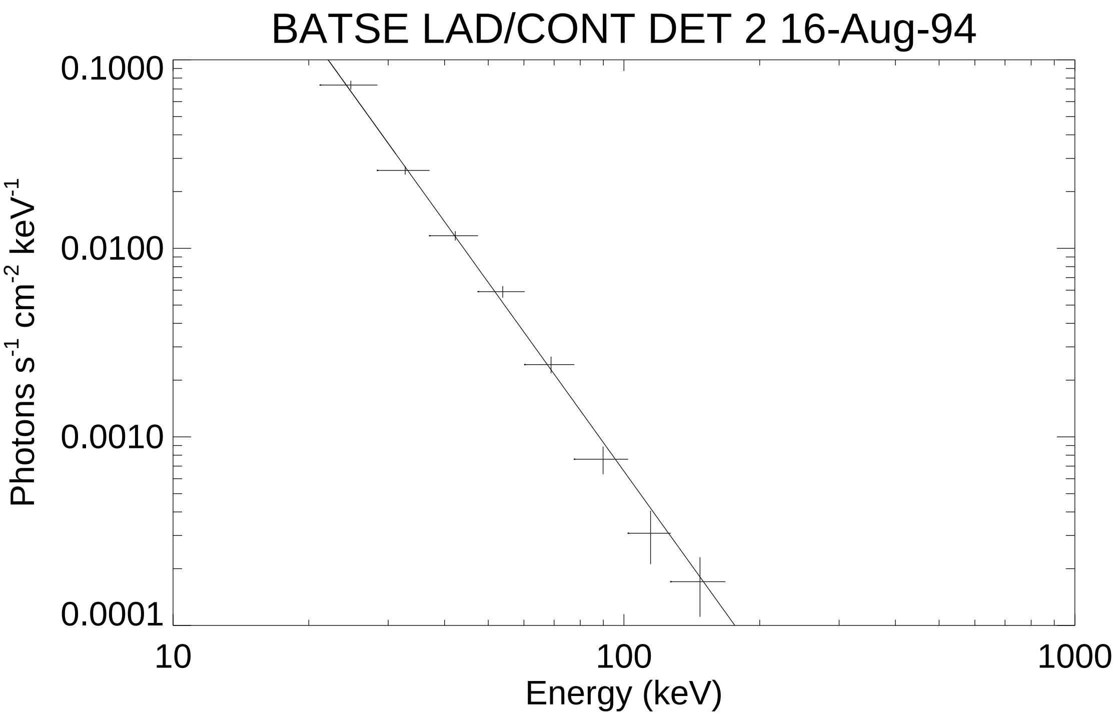

Fig. 6.— BATSE/LAD/CONT photon energy spectrum during the impulsive phase. A power-law fit to the spectrum yields A=6.5×10^{-3} and γ=3.4. The energy range corresponding to each energy channel is plotted as a horizontal bar at the location of the measurement, with the vertical bar being the error bar for that channel; the power–law fit is shown as a straight line. There are no significant counts in channels above 130 keV.